A STATISTICAL COMPARISON BETWEEN GIBBS AND HERRICK-GIBBS ORBIT DETERMINATION METHODS

A Thesis

by

ARVIND SHANKAR KAUSHIK

Submitted to the Office of Graduate and Professional Studies of
Texas A&M University
in partial fulfillment of the requirements for the degree of

MASTER OF SCIENCE

Chair of Committee,	John Junkins
Committee Members,	John Hurtado
	Shankar Bhattacharyya
	Kohei Fujimoto
Head of Department,	Rodney D. W. Bowersox

August 2016

Major Subject: Aerospace Engineering

Copyright 2016 Arvind Shankar Kaushik

ABSTRACT

The detection, tracking, identification, and characterization (DTIC) of resident space objects (RSOs) is an important aspect of space situational awareness (SSA). Monitoring the space environment can prevent collisions and eliminate hazards for spacecraft, as well as help enforce norms in the on-orbit regime. Consequently, there is a strong need for accurate RSO state estimates. For radar measurements of RSOs, these estimates are initiated by algorithms such as Gibbs and Herrick-Gibbs. Both methods use a track containing three sets of position vector (i.e., range + bearings) observations to analytically compute the objects' velocity at the time of the second observation.

Presently, there is no clear distinction on when to switch between these two methods. In this paper, we present a statistical comparison between Gibbs and Herrick-Gibbs, taking into account measurement errors. We implement two separate approaches to investigate this problem. The first approach is via Monte Carlo. We add Gaussian white noise at several iterations and evaluate Gibbs and Herrick-Gibbs performances over track length. The second approach is an analytic probability density function approach used to characterize the uncertainty of the Herrick-Gibbs state estimate.

We observe that the overall trend of the performance of the methods is consistent with what is expected. However, the results also show that Herrick-Gibbs can remain the more accurate method for much larger track lengths than is suggested in the literature. This is shown by both numerical and analytic statistical error analysis.

To my family and friends

ACKNOWLEDGEMENTS

Firstly, I'd like to thank my advisors Dr. Junkins and Dr. Hurtado for their insight and wisdom throughout my time at Texas A&M. I would also like to thank Dr. Kohei Fujimoto who has been my mentor on this work and whose guidance has been invaluable. Thank you to Dr. Alfriend whose course on Space Situational Awareness was the inspiration for this work. Thank you also to Dr. Bhattacharyya for being on my committee and Dr. Datta for attending my defense in his place. Thanks to my fellow graduate students at the LASR lab. Finally, I would like to thank my friends and family for their continued support and encouragement.

TABLE OF CONTENTS

Page

LIST OF FIGURES

FIGURE Page

LIST OF TABLES

TABLE Page

CHAPTER I

INTRODUCTION

There is a strong need for accurate resident space object (RSO) state estimates. Monitoring the space environment is an important aspect of space situational awareness (SSA). Precise tracking of RSOs can prevent collisions and eliminate hazards for spacecraft, as well as help enforce norms in the on-orbit regime [1]. Consequently, there is a strong need for accurate RSO state estimates. For radar measurements of RSOs, these estimates are initiated by algorithms such as Gibbs and Herrick-Gibbs [2]. Both methods use a track containing three sets of position vector (i.e., range + bearings) observations to analytically compute the object's velocity at the time of the second observation.

I.A. Problem Statement

Gibbs and Herrick-Gibbs are two frequently used initial orbit determination (IOD) methods. IOD is needed when a satellite has been launched or when a new object is detected. Once IOD has been performed, precise orbit determination can then be used to predict the orbit into the future as needed [3]. Thus, more accurate IOD will give more precise propagation. The problem is that there is not a clear distinction on when to switch between the aforementioned two methods. In Vallado, Gibbs is recommended for track arcs longer than 5°, and Herrick-Gibbs for track arcs shorter than 1°. These numbers, however, do not take into account measurement errors or orbit parameters of the target object. There thus needs to be a holistic, quantitative study on when to use one method over the other. We investigate this issue in this dissertation, as outlined in the thesis statement:

Herrick-Gibbs is the more accurate IOD method for longer track lengths than was previously known. This is shown by both numerical and analytic statistical error analyses.

I.B. Background

I.B.1. Gibbs Method

Gibbs method was proposed in 1889 by Josiah Gibbs. It uses three position vectors, and a geometric approach to determine the velocity of the middle position [4]. There are two major assumptions used for Gibbs method: the three position vectors are time sequential and co-planar. This second assumption can be somewhat relaxed as it is expected for measurement errors to cause the position vector's inclinations to vary slightly. Gibbs method is similar to the Gauss IOD method which utilizes the same assumptions and has the same first few steps. As stated by Vallado [5], Gibbs method should work well when the track length between the position vectors is greater than 5°. Using three time sequential position vectors $(\mathbf{r}_1, \mathbf{r}_2, \mathbf{r}_3)$, Gibbs method defines the three vectors

$$\mathbf{N} = r_1(\mathbf{r}_2 \times \mathbf{r}_3) + r_2(\mathbf{r}_3 \times \mathbf{r}_1) + r_3(\mathbf{r}_1 \times \mathbf{r}_2) \tag{1.1}$$

$$\mathbf{D} = \mathbf{r}_1 \times \mathbf{r}_2 + \mathbf{r}_2 \times \mathbf{r}_3 + \mathbf{r}_3 \times \mathbf{r}_1 \tag{1.2}$$

$$\mathbf{S} = \mathbf{r}_1(r_2 - r_3) + \mathbf{r}_2(r_3 - r_1) + \mathbf{r}_3(r_1 - r_2). \tag{1.3}$$

The estimated velocity of the middle observation, $\mathbf{v}_2$, is then defined as

$$\mathbf{v}_2 = \sqrt{\frac{\mu}{ND}} \left[\frac{\mathbf{D} \times \mathbf{r}_2}{r_2} + \mathbf{S} \right]. \tag{1.4}$$

A detailed derivation of the Gibbs method is shown in Appendix B [5] [6].

I.B.2. Herrick-Gibbs Method

When the track lengths between the position vectors are very small, the three vectors are almost parallel, so observation errors will likely degrade the determination of the orbit plane. Hence, Sam Herrick proposed the Herrick-Gibbs method which applies a power series of the two-body solution flow to the Gibbs method [7]. Herrick-Gibbs was not intended to be a generally applicable method, but rather only to be used when the track length is too short for an accurate Gibbs result. Defining Δt_{ij} as the difference between times of observations i and j, the following expression for $\mathbf{v}_2$ may be derived

$$\mathbf{v}_2 = -\Delta t_{32}\left[\frac{1}{\Delta t_{21}\Delta t_{31}} + \frac{\mu}{12r_1^3}\right]\mathbf{r}_1 + (\Delta t_{32} - \Delta t_{21})\left[\frac{1}{\Delta t_{21}\Delta t_{32}} + \frac{\mu}{12r_2^3}\right]\mathbf{r}_2 + \Delta t_{21}\left[\frac{1}{\Delta t_{32}\Delta t_{31}} + \frac{\mu}{12r_3^3}\right]\mathbf{r}_3. \quad (1.5)$$

A detailed derivation of the Herrick-Gibbs method is shown in Appendix B [8].

I.B.3. Transition Point

Since it is known that Gibbs works better for longer tracks and Herrick-Gibbs works better for shorter tracks, there must be a transition point that dictates which method will provide a more accurate solution. As the track length between radar observations increases, there will eventually be a track length value at which Gibbs and Herrick-Gibbs provide an equally accurate solution. For track lengths above this transition point, Gibbs will provide the better estimate and for track lengths below the transition point, Herrick-Gibbs will provide the better estimate. The transition point is visualized in Figure I.1. Determining the transition point is a key focus of this investigation.

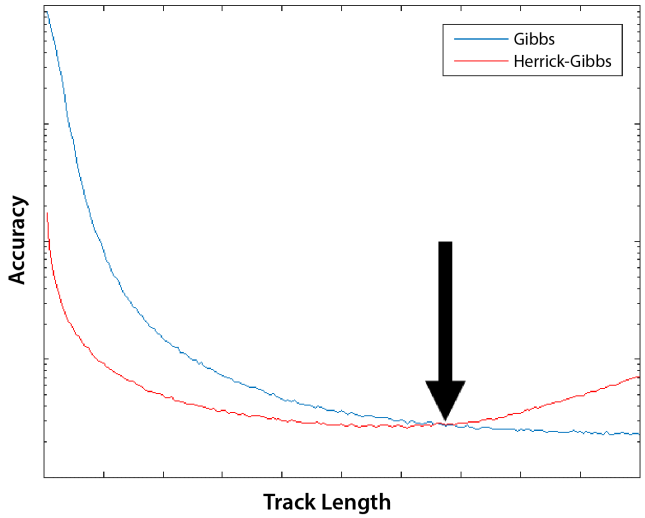

Figure I.1. Track length transition point. As Gibbs and Herick-Gibbs accuracies change over track length, there will be a value at which both methods produce an equally accurate estimate. This is defined as the transition point

I.C. Contributions

In our work, we present a holistic, quantitative study of IOD accuracy between Gibbs and Herrick-Gibbs. In this thesis, we present two methods for statistical comparisons of IOD accuracy between Gibbs and Herrick-Gibbs, taking into account measurement error for different observation geometries and target orbits. These are a Monte Carlo approach and an analytic probability density function (PDF) approach.

I.D. Literature Review

Previous research has compared IOD methods to evaluate what scenarios they are best suited for. Most of this work has been directed to angles-only orbit determination methods, such as the Gauss method. Taff acknowledges the popularity of the Gauss orbit determination method but rejects it in favor the Laplace method for gen-

eral cases [9]. Taff, Randall, and Stansfield expand upon this finding and give specific scenarios when Laplace should be used over Gauss [10]. In later work, Taff cautions against using the Laplace method when possessing only a small amount of data [11]. Celletti and Pinzari also compared the Laplace and Gauss methods [12] [13]. However, they concluded the Gauss method performed better in general. Additional comparisons between angles-only orbit determination methods were conducted by Fadrique et al [14]. They compared the Gauss, Gooding, and Baker Jacoby methods. They concluded that, in general, the Gooding algorithm performs better than the rest, although there are specific situations in which Gauss and/or Baker-Jacoby produce better results. A very comprehensive IOD analysis has been performed by Schaeperkoetter [3]. Schaeperkoetter tests Laplace, Gauss (using Gibbs and Herrick-Gibbs to supplement), the Double R, and the Gooding methods. He concludes that, in almost all cases, the Gooding method best estimates the orbit. The exception is for polar orbits in which it depends on the observation interval whether one uses the Gooding or Double R methods.

It was Foster [15] who directly compared the Gibbs and Herrick-Gibbs methods. He compared Gibbs and Herrick-Gibbs performances at 1° and 5° track lengths using two types of radar. At 1°, he found that Herrick-Gibbs was the more accurate method which was expected. At 5°, however he found that Herrick-Gibbs was better for one of the radars, and in the second it was less than 1% different than the Gibbs. He acknowledged that this was a surprising result. We can expand upon these results with a much more comprehensive comparison between the two methods.

CHAPTER II

STATISTICAL ANALYSIS

The objective of this research will be achieved in two separate statistical analyses. The first part is a computational comparison using Monte Carlo, and the second part will be an analytic solution from a derived partial density function (PDF).

II.A. Monte Carlo Analysis

For the Monte Carlo analysis, we implement measurement errors to observe how Gibbs and Herrick-Gibbs performance change as track length is varied. We performed two types of tests: Test 1 and 2. In Test 1, we vary track arclength so as to determine the track length transition point at which the more accurate IOD method switches. Both the observer and the target orbit apse line are fixed such that the second observation takes place at zenith and at periapsis. Tracks symmetric about this second observation as well as asymmetric tracks are analyzed separately. For each track arclength, we consider 1,000 instantiations of Gaussian white noise measurement error, which are added to the measurements in the topocentric spherical coordinates. Finally, we determine the transition point based on the mean results. These tests are repeated for five target objects: GeoEye-1, the Hubble Space Telescope, the International Space Station, a Molniya orbit, and a generic geostationary spacecraft. In Test 2, we evaluated the sensitivity of the aforementioned transition point to orbital parameters and observer location. That is, the transition point is determined as the semi-major axis and eccentricity of the target orbit are changed individually. The effects of measurement errors are again assessed with 1,000 Monte Carlo samples.

II.B. Analytic PDF Analysis

To validate our Monte Carlo results, we implemented an analytic PDF method. The goal is to derive a probability density function for a state estimate determined by Herrick-Gibbs. The PDF is a direct representation of how Herrick-Gibbs maps measurement errors to the uncertainty of the state. Since Herrick-Gibbs takes three position vectors as inputs to estimate the velocity of the middle position vector, we need to represent the joint state estimate PDF $p(\dot{\mathbf{r}}_2, \mathbf{r}_2)$ from the joint position vector PDF $p(\mathbf{r}_1, \mathbf{r}_2, \mathbf{r}_3)$.

The main source of this method comes from a paper and dissertation by Ryan Weisman [16]. Weisman presents an analytic approach to derive a PDF for a state estimate determined by the Herrick-Gibbs method.

II.B.1. Transformation of Variables

The transformation of variables (TOV) method allows for a known PDF to be mapped from one domain to another [17]. Equation (2.1) shows how the TOV method can be used to map a PDF from the y-domain to the x-domain. $p(y)$ is multiplied by the inverse of the determinant of the absolute value of the Jacobian of y with respect to x.

$$p(x) = p(y)|J|^{-1} \tag{2.1}$$

The TOV method can be used to determine the joint PDF of our observed position vectors, $p(\mathbf{r}_1, \mathbf{r}_2, \mathbf{r}_3)$. First, using the assumption that our three position vectors are independent, Equation (2.2) shows how we can express a joint PDF based on the individual distributions of range, azimuth, and elevation.

$$p(\tilde{\mathbf{z}}_1, \tilde{\mathbf{z}}_2, \tilde{\mathbf{z}}_3) = \prod_{i=1}^{3} p(\rho_i)p(el_i)p(az_i) \tag{2.2}$$

$$|J_i| = \left| \frac{\partial \mathbf{r}_i}{\{\rho,\, el,\, az\}_i} \right| = \rho^2 \cos(el) \tag{2.3}$$

We assume a Gaussian distribution for the range and bearings based on the measurement errors used in the Monte Carlo analysis. Equation (2.3) shows the determinant of the absolute value of the Jacobian based on the partial derivatives of the range and bearings with respect to the position vectors. Using the TOV approach, the position vector joint PDF is evaluated based on the joint PDF of the range and bearings and the inverse of the determinant.

$$p(\mathbf{r}_1, \mathbf{r}_2, \mathbf{r}_3) = \left[p(\tilde{\mathbf{z}}_1, \tilde{\mathbf{z}}_2, \tilde{\mathbf{z}}_3) \prod_{i=1}^{3} |J_i|^{-1} \right]_{\mathbf{z}=f(\mathbf{r}_i)} \tag{2.4}$$

II.B.2. Dirac Delta Method

The Herrick-Gibbs method uses three position vectors to determine the state at the second epoch. Since this not a one-to-one mapping (we are mapping three states into two), the Jacobian will be non-square, which poses an issue for the TOV method. This can be resolved by using the Dirac generalized function [18]. The Dirac delta, also known as the impulse function, can be related to the PDF by the following theorem:

Theorem 1: Suppose that z_i, $i = [1, n]$, are continuous random variables with joint probability distribution $p(z_1, z_2, ..., z_n)$. Let D be the n-dimensional set of every possible outcome of the z_i. Then the continuous random variable

$$x = \psi^{-1}(z_1, z_2, ..., z_n)$$

has the probability distribution given by use of the Dirac generalized function $\delta(x)$ in the form

$$p(x) = \int_{D^z} p(z_1, z_2, ..., z_n)\, \delta\left[\psi^{-1}(z_1, z_2, .., z_n) - x\right]\, \mathrm{d}z_1 \mathrm{d}z_2 ... \mathrm{d}z_n \tag{2.5}$$

We can make use of the composition and translation properties of the Dirac delta function to simplify the expression:

Composition Property:

$$\delta[f(y)] = \sum \delta(y - y_n) \left| \frac{\partial f(y)}{\partial y} \right|^{-1} \tag{2.6}$$

Translation Property:

$$\delta[f(y)] = \int_{-\infty}^{\infty} f(y)\, \delta(y - a) \mathrm{d}y \tag{2.7}$$

II.B.3. Example

To illustrate the Dirac delta method, here is an example of a 2-D circle defined by radius ρ and angle α from Weisman [16]. The x, y coordinates on the circle can be defined by these two parameters.

$$\rho = \sqrt{x^2 + y^2} \tag{2.8}$$

$$\alpha = \arctan\left[\frac{x}{y}\right] \tag{2.9}$$

The PDF for x based on the distributions of ρ and α is a two-to-one mapping, and thus, an ideal candidate to implement Theorem 1.

An expression for the PDF of x is shown in Equation (2.10).

$$p(x) = \int_{D^\rho} \int_{D^\alpha} p(\rho, \alpha)\, \delta[\rho \cos(\alpha) - x]\, \mathrm{d}\rho\, \mathrm{d}\alpha \tag{2.10}$$

This expression can be simplified using the composition and translation properties:

$$p(x) = \int_{D^\rho} \int_{D^\alpha} \frac{p(\rho, \alpha)}{\rho \sin\alpha}\, \delta\left[\alpha - \arccos\left(\frac{x}{\rho}\right)\right] \mathrm{d}\rho\, \mathrm{d}\alpha \quad \textbf{... Composition} \tag{2.11}$$

$$= \int_{\rho_0}^{\rho_f} \left| \frac{1}{\rho \sin\alpha} \right| \left[p(\rho = \rho, \alpha = \arccos\left(\frac{x}{\rho}\right)\right] \mathrm{d}\rho \quad \textbf{... Translation} \tag{2.12}$$

CHAPTER III

METHODOLOGY

In this section, we outline the approach we used to conduct our analysis. The accuracy of IOD methods for angles-only observations has been compared before [10], but here we present our own method of comparing Gibbs and Herrick-Gibbs performance.

III.A. Monte Carlo Approach

As previously mentioned, we conducted two types of tests. In Test 1, we analyze how performance changes with respect to both symmetric and asymmetric track lengths. In Test 2, we quantify how orbital elements and measurement error can affect performance through a sensitivity analysis.

III.A.1. Test 1

We used the following approach to test the accuracy of Gibbs and Herrick-Gibbs as a function of track length. This approach provides a way to quantify the Gibbs / Herrick-Gibbs track length transition point. We use the two IOD algorithms to estimate the velocity of the middle position at each track length for a known orbit. We then determine the deviation between the estimated velocity and the true velocity. Here are the steps in detail.

1. **Define a known orbit and observer location** A specific orbit is defined as the target object, whose position and velocity vectors shall be determined. The observer location is then determined to be directly below the object at

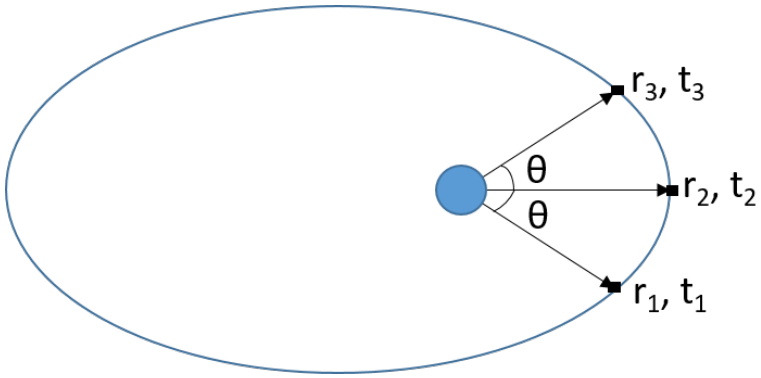

Figure III.1. Earth and its target orbit. The 3 observed position vectors ($\mathbf{r}_1$, $\mathbf{r}_2$, $\mathbf{r}_3$) and their respective times of observation (t_1, t_2, t_3). The track length θ is symmetric about the middle observation, which is directly above the observer at perigee.

perigee, at which point the object will appear to be at zenith.

2. **Determine position vectors, times of observation, and true velocity** The track length, or the angle between measurements, is then varied symmetrically from the observer to provide three position vectors ($\mathbf{r}_1$, $\mathbf{r}_2$, and $\mathbf{r}_3$). $\mathbf{r}_2$, the middle position vector, remains constant at perigee as track length is varied. Orbital mechanics equations based on two-body dynamics can determine the true positions, velocities and observation times based on the track length, which is analogous to the change in true anomaly. This point is illustrated in Figure III.1.

3. **Run 1,000 tests for each track length** For each set of position vectors, 1,000 Monte Carlo iterations are run to introduce Gaussian measurement noise at each track length. The measurement errors are 0.015° 1-σ for the azimuth and elevation, and 30 meters 1-σ for the range [5]; they are assumed to be uncorrelated. To introduce error to the range, azimuth, and elevation, the line-of-sight vectors need to be determined from the position vectors and observer

locations. The line-of-sight vectors are then brought to the topocentric-horizon or SEZ coordinates, at which the errors can be directly added to the range and bearings. From there, the error affected position vectors in the Earth-centered inertial frame are determined.

4. **Determine $\mathbf{v}_2$ from Gibbs and Herrick-Gibbs** At each iteration, Gibbs and Herrick-Gibbs use the three error affected position vectors to estimate $\mathbf{v}_2$. Both methods follow the procedures discussed earlier and are repeated at each track length.

5. **Determine velocity deviation magnitude** To quantify the accuracy of the estimated $\mathbf{v}_2$, the estimated value needs to be compared to the true value. The parameter d is introduced and defined as the magnitude of the deviation between the true and estimated velocities

$$d = \|\mathbf{v}_{2,\text{estimate}} - \mathbf{v}_{2,\text{actual}}\| \tag{3.1}$$

   There should be 1,000 results for d at each track length.

6. **Plot d versus track length** From there, a plot of the mean value of d vs. track length can be made to show how Gibbs and Herrick-Gibbs performance varies over track length. The track length at which the Gibbs and Herrick-Gibbs curves intersect will be the aforementioned transition point. These steps are then repeated for different orbits to compare results. Furthermore, this approach can be continuously repeated as parameters such as orbital elements and observer location are changed to see what effect they have on the transition point.

These steps can be visualized in the flowchart shown in Figure III.2. This

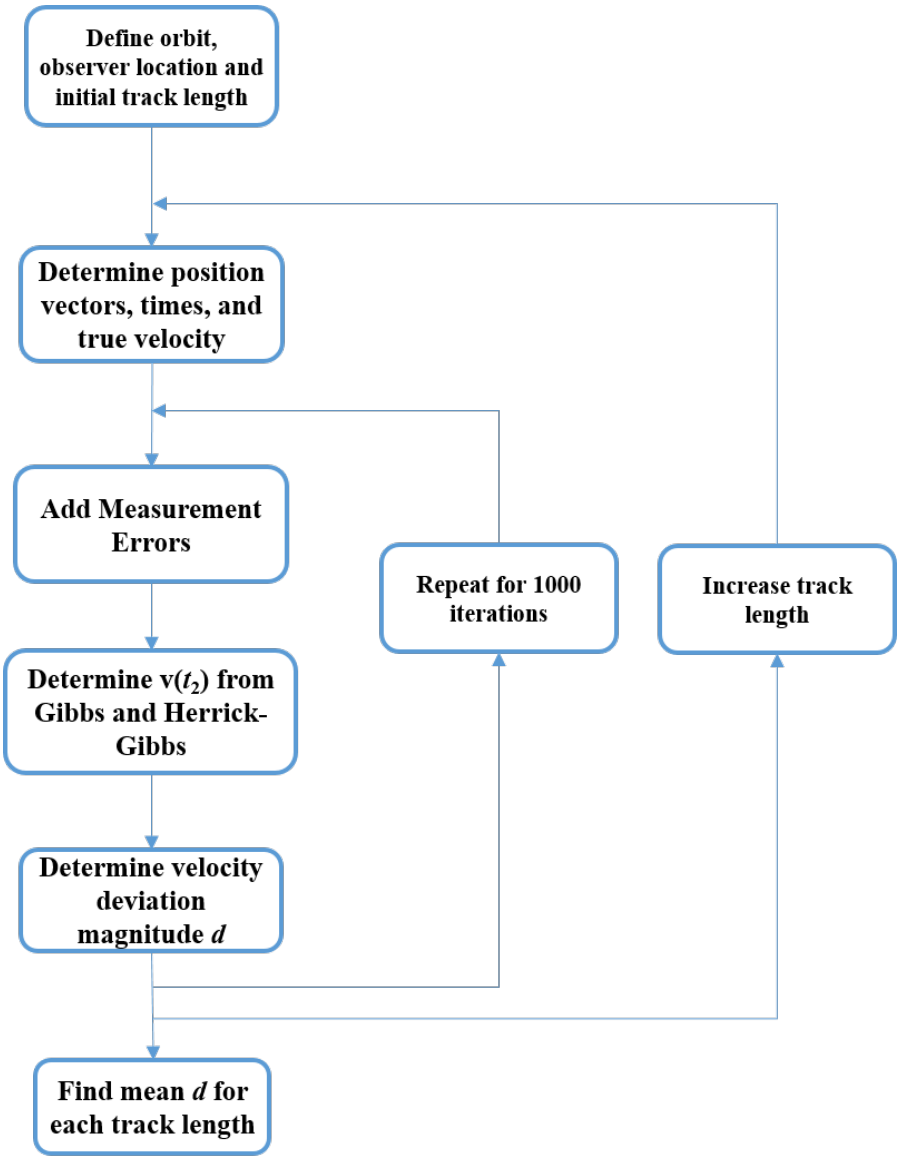

Figure III.2. Flowchart outlining the steps to conduct Test 1 of the Monte Carlo Analysis

procedure outlined was tested for five orbits. The orbits and their Keplerian orbit elements are

- ISS ($a = 6778$ km, $e = 0.0005818$, $i = 51.65°$, $\omega = 212.054°$, $\Omega = 45.14°$)
- GeoEye-1 ($a = 7057$ km, $e = 0.0008018$, $i = 98.11°$, $\omega = 279.6°$, $\Omega = 168.5°$)
- Molniya ($a = 26610$ km, $e = 0.722$, $i = 63.4°$, $\omega = -90°$, $\Omega = 0$)
- Hubble ($a = 6924$ km, $e = 0.0003128$, $i = 28.4693°$, $\omega = 52.6829°$, $\Omega = 130.3495°$)
- Geostationary orbit ($a = 42241$ km, $e = 0$, $i = 0$, $\omega = 0$, $\Omega = 0$).

Additionally, we extended our methods to examine the accuracy of Gibbs and Herrick-Gibbs algorithms for the case of asymmetric tracks, as in most cases, it cannot be expected that an object will be observed at equally spaced intervals. In this procedure, we considered two separate track lengths: θ_1, the angle between the first and second observations, and θ_3, the angle between the second and third observations. We tested 100 iterations at each θ_1-θ_3 combination from 0 to 90 degrees. We then performed the same Gibbs and Herrick-Gibbs analysis as before – adding Gaussian white noise for each iteration and determining the deviation between the true and estimated velocities – and recorded the number of iterations that Herrick-Gibbs had a lower value of d than Gibbs. If, for instance, Herrick-Gibbs outperformed Gibbs for all 100 iterations, one may conclude that the former is the preferred option, and vice versa.

III.A.2. Test 2

It would useful to determine how continuous changes to individual inputs would affect the Gibbs / Herrick-Gibbs transition point. To test this, we repeated Test

1 for symmetric tracks but varying a given orbital element – semi-major axis or eccentricity – or measurement noise standard deviation.

To evaluate the effects of orbital parameters, we repeated our analysis for 20 linearly spaced values of semi-major axis between 7,000 and 50,000 km. We then did the same for 20 linearly spaced values of eccentricity between 10^{-5} and 0.7. From this, we aim to see how Gibbs and Herrick-Gibbs performance are affected by these parameters. The 1,000 Monte Carlo instantiations of measurement noise will be run for each input to determine the mean transition point between the Gibbs and Herrick-Gibbs results. We also introduce a new metric to evaluate the performance of each method. Since velocity changes significantly with respect to orbital elements, we can't rely on the absolute error. Instead we normalize by the true velocity at periapsis. The new parameter $d2$ is:

$$d2 = \frac{\|\mathbf{v}_{2,\text{estimate}} - \mathbf{v}_{2,\text{actual}}\|}{\|\mathbf{v}_{2,\text{actual}}\|} \tag{3.2}$$

We also performed an error sensitivity analysis to see what effect measurement error size has on our results. We tested 25 different combinations of range and azimuth / elevation error and repeated our analysis to determine the Gibbs / Herrick-Gibbs transition point at each case. From our results, we can determine how sensitive the transition point is to different error magnitudes.

III.B. PDF Approach

To validate the results found by Monte Carlo, we also want to implement an analytic PDF approach. We want to develop a PDF for the Herrick-Gibbs state estimate, $p(\dot{\mathbf{r}}_2, \mathbf{r}_2)$ based on the joint PDF of the position vectors using TOV.

Since Herrick-Gibbs is over constrained, we will get a non-square Jacobian, preventing us from directly implementing the TOV. To get around this issue, we invoke

the Dirac delta method [16].

III.B.1. Dirac Delta Method

Using the properties of the Dirac delta function, we can create an expression for the state estimate PDF. Using Theorem 1, we can determine an expression for the Herrick-Gibbs state estimate:

$$p(\mathbf{r}_2, \dot{\mathbf{r}}_2) = \iint p(\mathbf{r}_1, \mathbf{r}_2, \mathbf{r}_3)\, \delta[HG(\mathbf{r}_1, \mathbf{r}_2, \mathbf{r}_3) - \dot{\mathbf{r}}_2]\, \mathrm{d}\mathbf{r}_1 \mathrm{d}\mathbf{r}_2 \mathrm{d}\mathbf{r}_3 \tag{3.3}$$

This expression is too complicated to evaluate directly, so we invoke Dirac delta properties to simplify the expression and eliminate the delta expression. The composition property (2.6) lets us simplify the delta expression in the integral:

$$\delta[HG(\mathbf{r}_1, \mathbf{r}_2, \mathbf{r}_3) - \dot{\mathbf{r}}_2] = \left| \frac{\partial \dot{\mathbf{r}}_2}{\partial \mathbf{r}_3} \right|^{-1}_{\mathbf{r}_3 = g_{32}} \delta(\mathbf{r}_3 - g_{32}) \tag{3.4}$$

where g_{32} is the root of the Herrick-Gibbs expression with respect to $\mathbf{r}_3$. g_{32} is an expression of $\mathbf{r}_3$ in terms of $\mathbf{r}_1$, $\mathbf{r}_2$ and $\dot{\mathbf{r}}_2$. $\mathbf{r}_3$ needs to be approximated using the F and G series [16] because of the complexity in evaluating the root for $\mathbf{r}_3$. The analytic expressions for F and G are based on a Taylor series approximation and shown in Equations (3.5)-(3.10).

$$\mathbf{r}_3 = g_{32}(\dot{\mathbf{r}}_2, \mathbf{r}_2, \mathbf{r}_1) = \frac{\dot{\mathbf{r}}_2 - t_{23}\left(\frac{1}{t_{21}t_{31}} + \frac{\mu}{12 r_1^3}\right)\mathbf{r}_1 - (t_{32} - t_{21})\left(\frac{1}{t_{21}t_{32}} + \frac{\mu}{12 r_2^3}\right)\mathbf{r}_2}{t_{21}\left(\frac{1}{t_{31}t_{32}} + \frac{\mu}{12}|F_{32}\mathbf{r}_2 + G_{32}\dot{\mathbf{r}}_2|^{-3}\right)} \tag{3.5}$$

$$F_{i2} = 1 - \frac{\tau_{i2}^2}{2}\epsilon + \frac{\tau_{i2}^3}{2}\epsilon\lambda - \frac{\tau_{i2}^4}{24}(15\epsilon\lambda^2 - 3\epsilon\psi + 2\epsilon^2) + ... \tag{3.6}$$

$$G_{i2} = \tau_{i2} - \frac{\tau_{i2}^3}{6}\epsilon + \frac{\tau_{i2}^4}{4}\epsilon\lambda + ... \tag{3.7}$$

$$\epsilon = \mu(\mathbf{r}_2^{\mathrm{T}}\mathbf{r}_2)^{-3/2} \tag{3.8}$$

$$\lambda = (\mathbf{r}_2^{\mathrm{T}}\mathbf{r}_2)^{-1}(\mathbf{r}_2^{\mathrm{T}}\dot{\mathbf{r}}_2) \tag{3.9}$$

$$\psi = (\mathbf{r}_2^{\mathrm{T}}\mathbf{r}_2)^{-1}(\dot{\mathbf{r}}_2^{\mathrm{T}}\dot{\mathbf{r}}_2) \tag{3.10}$$

The τ terms correspond to the times of observations for the objects. With these approximations, we can simplify our state estimate PDF:

$$p(\mathbf{r}_2, \dot{\mathbf{r}}_2) = \iint p(\mathbf{r}_1, \mathbf{r}_2, \mathbf{r}_3) \left| \frac{\partial \mathbf{r}_2}{\partial \mathbf{r}_3} \right|^{-1}_{\mathbf{r}_3 = g_{32}} \delta(\mathbf{r}_3 - g_{32}) \, \mathrm{d}\mathbf{r}_1 \mathrm{d}\mathbf{r}_3 \tag{3.11}$$

We can then use the translation property to eliminate the delta expression completely and simplify the integration. We now have a form of the PDF we can directly evaluate.

$$p(\mathbf{r}_2, \dot{\mathbf{r}}_2) = \int \left| \frac{\partial \mathbf{r}_2}{\partial \mathbf{r}_3} \right|^{-1}_{\mathbf{r}_3 = g_{32}} p(\mathbf{r}_1, \mathbf{r}_2, \mathbf{r}_3 = g_{32}) \, \mathrm{d}\mathbf{r}_1 \tag{3.12}$$

III.B.2. Analytic PDF Evaluation

Now that we have an expression for the Herrick-Gibbs state estimate PDF, we can evaluate this PDF for each component of $\dot{\mathbf{r}}_2$ with the following steps.

1. **Define a known orbit and observer location** As with the Monte Carlo, the first step is to fully define an orbit and observer location. We also define a constant track length value. We determine the true position vectors and observation times based on two-body orbital mechanics equations. Once again, the observer is located directly below the middle observation, which is at perigee.

   The PDF is integrated over the range of $\mathbf{r}_1$ domain. We determine the practical limits of integration based on results obtained from Monte Carlo. We also determine the mean $\dot{\mathbf{r}}_2$, range, azimuth and elevation values.

2. **Vary $\dot{\mathbf{r}}_2$** We then vary the $\dot{\mathbf{r}}_2$ components to see how the PDF value changes with respect to each $\dot{\mathbf{r}}_2$ component. We vary one component at a time; i.e., while we vary $\dot{x}_2$, $\dot{y}_2$ and $\dot{z}_2$ are held constant at their mean values. The limits of each $\dot{\mathbf{r}}_2$ component are determined via Monte Carlo.

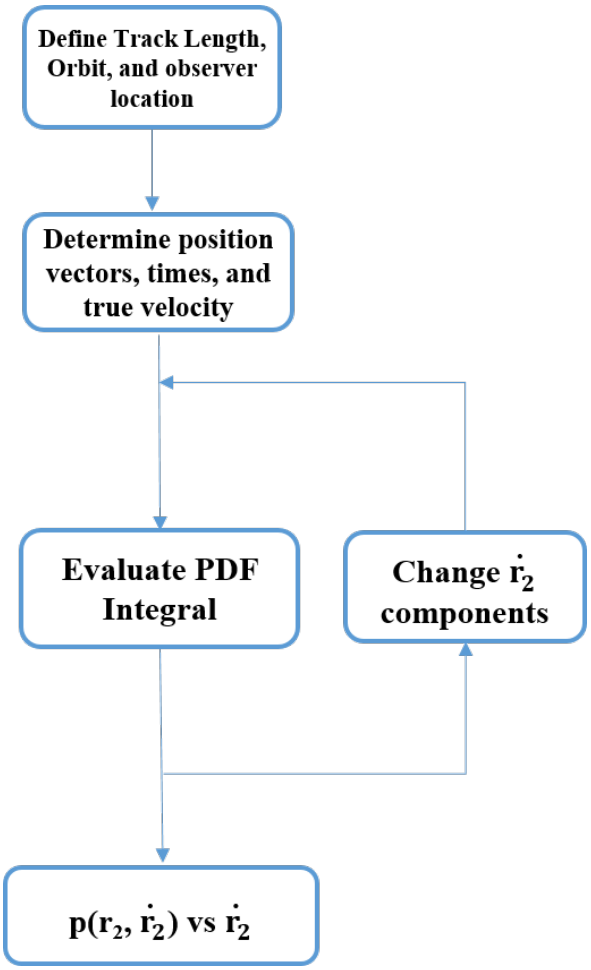

Figure III.3. Flowchart outlining the steps to evaluate the PDF analytically over the $\dot{r}_2$ components

3. Evaluate Integral We then evaluate the PDF integral by defining quadrature volumes and multiplying by the integrand value. We sum all the values over the limits of integration. We obtain a solution for the analytic pdf for each value of $\dot{\mathbf{r}}_2$.

These steps can be outlined in the flowchart shown in Figure III.3. We chose to implement this approach for the Hubble orbit at 5° track length. In this case, the mean $\mathbf{r}_2$ value is $[-6404.8129, 64.8310, 2.62411]$ km in ECI. We found the following range of $\mathbf{r}_1$ components from Monte Carlo, which are the limits of integration to

evaluate the PDF:

$$x_1 : [-6446.341, -6445.773] \tag{3.13}$$

$$y_1 : [637.556, 638.950] \tag{3.14}$$

$$z_1 : [2439.174, 2440.343] \tag{3.15}$$

III.B.3. Monte Carlo PDF Evaluation

We also want to evaluate the PDF numerically through Monte Carlo. The steps required are as follows.

1. **Define a known orbit and observer location** Once again, we start by defining our initial conditions. We specify a known orbit, track length and observer location. We can then determine the true states with two body orbital mechanics equations.

2. **Run 10^6 Monte Carlo Iterations** We then run one million Monte Carlo iterations to add Gaussian white noise to our position vectors at the specified orbit condition. As before, the errors we used were 0.015° 1-σ for azimuth/elevation and 30 m 1-σ for range.

3. **Estimate $\dot{\mathbf{r}}_2$ with Herrick-Gibbs** At each iteration, we implement Herrick-Gibbs to estimate $\mathbf{v}_2 = \dot{\mathbf{r}}_2$ from the three error affected position vectors.

4. **Filter results to emulate a 1-D PDF** Since our analytical PDF results are varied for one $\dot{\mathbf{r}}_2$ component at a time, we must ensure that the Monte Carlo results are similarly one-dimensional in the $\dot{\mathbf{r}}_2$ space. For example, when we evaluate the PDF value vs. $\dot{x}_2$, we only store the Monte Carlo values when all other states are close to their mean results. The tolerances were set as 4×10^{-4}

for $\dot{x}_2$ and $\dot{y}_2$; 5×10^{-4} for $\dot{z}_2$; 0.02 for x_1 and y_1; and 0.04 for z_1. We then plot a histogram of the MC outcomes as a function of $\dot{x}_2$.

These steps are visualized in the flowchart shown in Figure III.4.

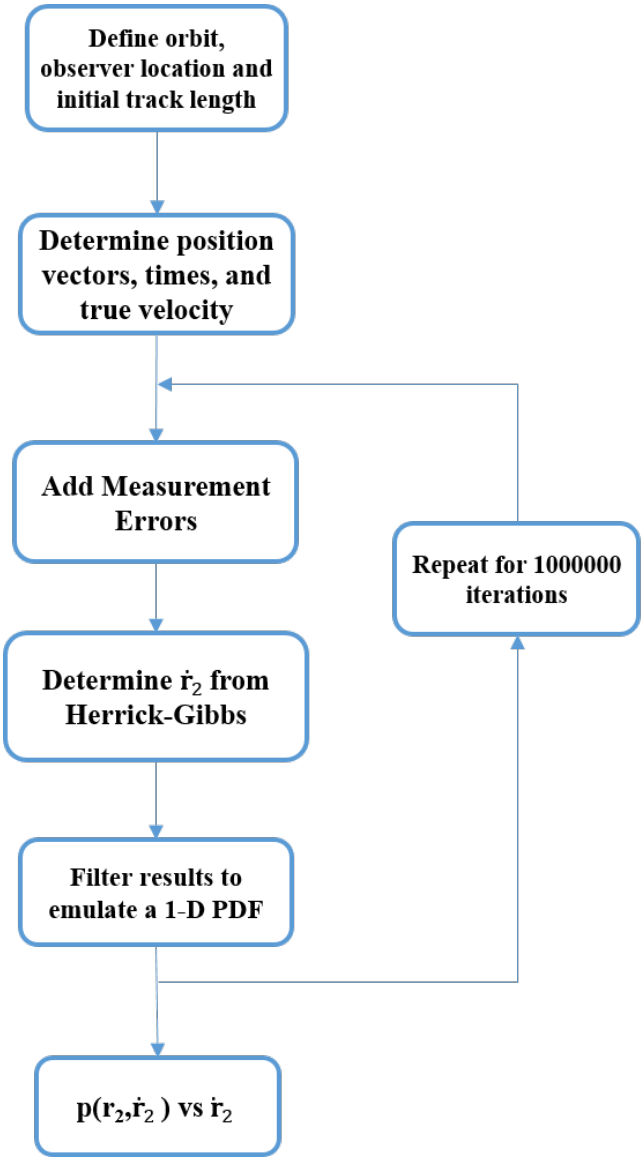

Figure III.4. Flowchart outlining the steps to evaluate the PDF via Monte Carlo

CHAPTER IV

RESULTS

In this section, we present the results obtained from our study. Only the main results for each test are highlighted; additional plots are available in Appendix A.

IV.A. Monte Carlo Results

IV.A.1. Test 1 - Symmetric Tracks

Figure IV.1 below shows the mean d vs. track length plot for the ISS from 5° to 90°. In reality, above a certain track length, the object will be below the horizon of the observer, but plotting to 90° nonetheless gives insight into IOD performance at large track lengths. Both Gibbs and Herrick-Gibbs follow the trends that are expected. Gibbs starts off with high error but quickly decreases for longer track lengths. Herrick-Gibbs, on the other hand, does the opposite, although it does not appear to level off like with Gibbs; in fact, Herrick-Gibbs has very high inaccuracy at large track lengths. If we examine the same plot but at a smaller track length range (0.1° to 20°) to get a better look at the transition point, we find that for the tested case, Herrick-Gibbs remains more accurate than Gibbs for up to about 14°: a value higher than expected. Although Herrick-Gibbs starts losing accuracy for tracks longer than 12°, it still remains more accurate than Gibbs.

Figures IV.2 shows the error bar plots for the ISS. For the Gibbs case, the bars remain approximately the same size at all track lengths. For Herrick-Gibbs, however, the bars start off similarly sized as Gibbs but become much smaller for longer track lengths. This result suggests that Herrick-Gibbs becomes insensitive to measurement

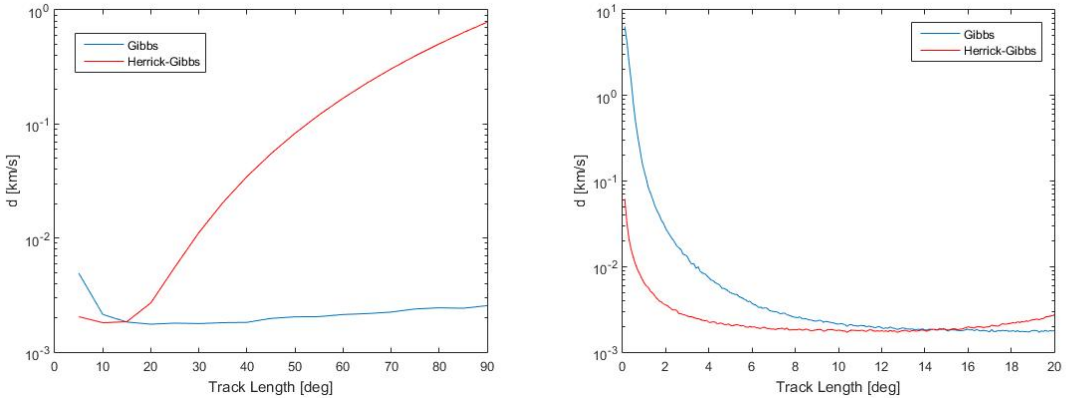

Figure IV.1. Log-y plot of mean d vs. track length for the ISS. The plot on the right is a zoomed up version of the plot on the left.

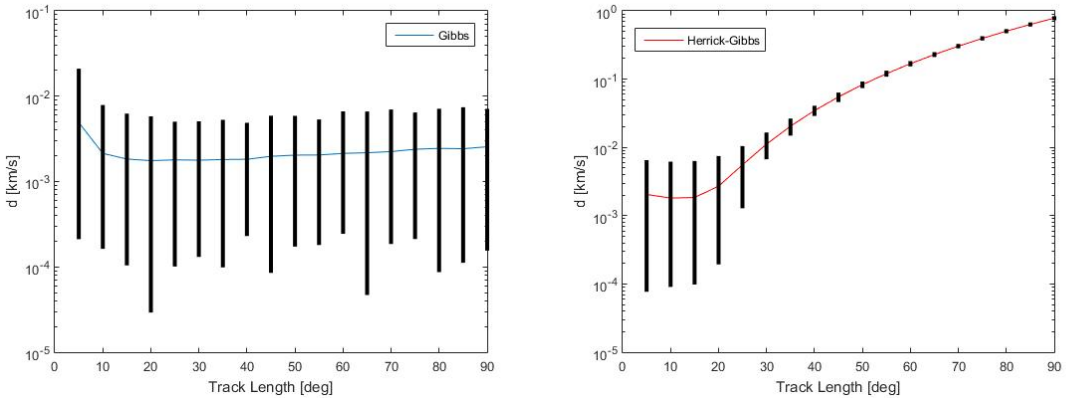

Figure IV.2. Error bar plots for the ISS for Gibbs (left) and Herrick-Gibbs (right) IOD. The lines represent the mean d value, where as bars represent the range of d values for each track length based on measurement error.

Table IV.1. Transition points for each orbit.

Orbit	Transition Point [deg]
ISS	14.4
GeoEye-1	15.2
Molniya	13.3
Geostationary	6.4
Hubble	14.3

errors for tracks longer than about 20°.

Similar results were found for all orbits tested. In all cases, Gibbs starts off less accurate than Herrick-Gibbs at short track lengths, but as track length increases, starts performing better and transitions to become the more accurate method for larger track lengths. The insensitivity of Herrick-Gibbs to measurement error for long tracks were also seen for all tested orbits.

Finally, one of our remaining objectives was to quantify the transition point that determines which method provides the better result. To reiterate, Herrick-Gibbs provides the more accurate estimate until the transition point is reached, after which Gibbs becomes the better method. Table IV.1 shows the transition track lengths determined for each orbit. In all cases, it's between 6° to 16°. Now that there is a way to evaluate the transition point for a known orbit, this procedure can be repeated as target and noise parameters are varied to see how the transition point changes. For instance, although the orbits with the largest semi-major axes (Molniya and Geostationary) have the smallest transition points, as we will see later, this result is not a general one.

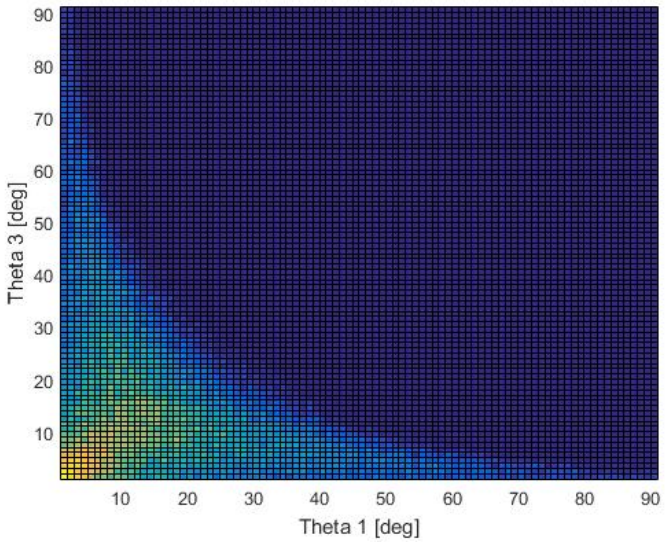

Figure IV.3. Pseudocolor plot representation of Gibbs and Herrick-Gibbs IOD performance for asymmetric tracks for GeoEye-1. The coloring of each block corresponds to the method that provided the more accurate result more consistently at each track length combination. Yellow blocks are when Herrick-Gibbs provided the more accurate result for all Monte Carlo iterations, and blue blocks are when Gibbs provided the more accurate result.

IV.A.2. Test 1 - Asymmetric Tracks

Figure IV.3 represents the results of the asymmetric track test. Each block on the pseudocolor plot represents one θ_1-θ_3 combination. The color represents the method that consistently provided the more accurate velocity estimate over 100 Monte Carlo iterations. Regions colored in green suggest that one method was not consistently the best for all iterations. There is a specific region in the plot where Herrick-Gibbs most frequently provides the best solution than Gibbs; i.e., when both track lengths are less than 18°. This result is consistent with the transition points we determined for symmetric tracks. Only at much smaller track lengths (less than 5°), however, can we expect Herrick-Gibbs to consistently deliver the best IOD solution every time.

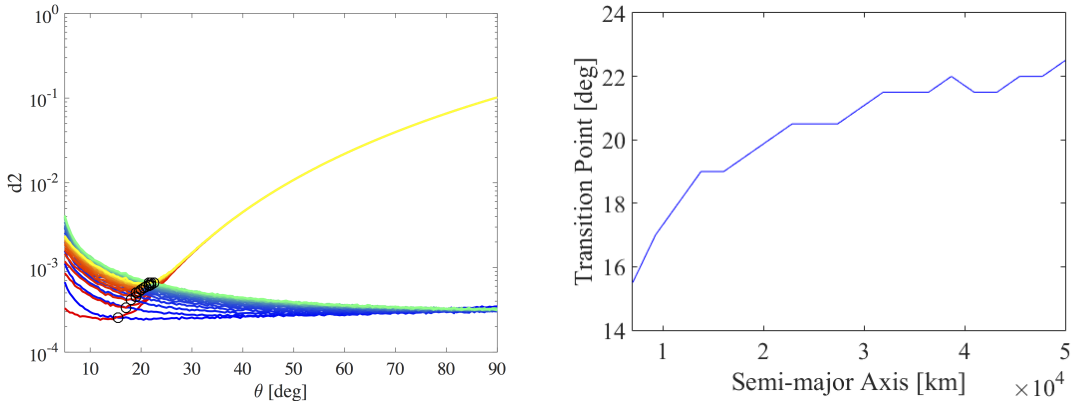

Figure IV.4. (Left) Initial orbit determination error as a function of track length for GeoEye-1. Cool colors indicate Gibbs results, whereas warm colors indicate Herrick-Gibbs results. Target semi-major axis increases as colors become lighter. Transition point indicated by black circles. (Right) Transition point of Gibbs / Herrick-Gibbs performance as a function of target semi-major axis.

IV.A.3. Test 2 - Sensitivity to Orbit Elements

Figure IV.4 simultaneously shows the results of 20 comparisons between Gibbs and Herrick-Gibbs as in the previous section, but the semi-major axis of the target object is altered between 7,000 km to 50,000 km. All other orbit elements are fixed to those of GeoEye-1. The transition point is highlighted with a black circle; a separate plot of the transition point as a function of semi-major axis is also given.

When the track length is short, both Gibbs and Herrick-Gibbs performance degrade for larger semi-major axis values since the line-of-sight error becomes more and more exaggerated. As track length increases, however, these errors become smoothed out, and thus the degradation is suppressed. Furthermore, when the target semi-major axis is greater than approximately 1.5×10^4 km, $d2$ starts to decrease for all track lengths. For these altitudes, the decrease in the output velocity magnitude has a larger effect on the absolute error than the line-of-sight error. The locus of the transition point in the $d2$-θ space is the result of a combination of these phenomena;

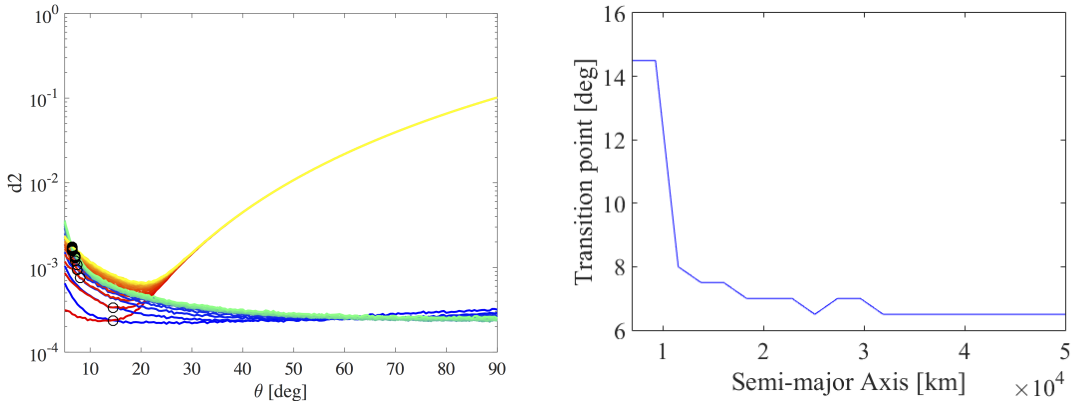

Figure IV.5. Similar to Figure IV.4, (Left) Initial orbit determination error as a function of track length for a geostationary satellite. (Right) Transition point of Gibbs / Herrick-Gibbs performance as a function of target semi-major axis.

as such, there is no general behavior for the transition point as a function of semi-major axis. For instance, Figure IV.5 is a similar analysis but for a geostationary satellite. Here, the transition point first occurs on the increasing segment of the Herrick-Gibbs $d2$-θ plot, but moves to the decreasing segment for semi-major axes over approximately 1.2×10^4 km. As such, in opposite fashion to Figure IV.4, the transition point is lower for higher semi-major axes.

Trends are similar for when the target eccentricity is changed, albeit in reverse as before because now the periapsis orbit radius decreases as eccentricity increases. In Figure IV.6, 20 values of eccentricity linearly spaced between 10^{-5} and 0.7 are substituted into the orbit elements for the Molniya orbit. The transition point locus remains on the decreasing segment of the Herrick-Gibbs $d2$-θ, so consequently, the transition point increases as eccentricity increases.

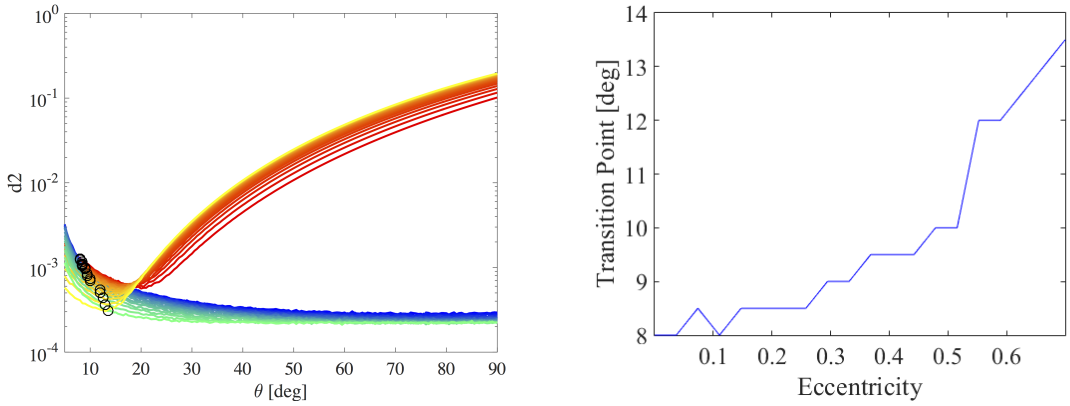

Figure IV.6. Similar to Figure IV.4, (Left) Initial orbit determination error as a function of track length for a Molniya satellite. Target eccentricity increases as colors become lighter. (Right) Transition point of Gibbs / Herrick-Gibbs performance as a function of target eccentricity.

IV.A.4. Test 2 - Sensitivity to Measurement Error

Figure IV.7 shows the transition points of the GeoEye-1 satellite for 25 combinations of range and angle errors. We tested 5 different range error magnitudes $\log_{10}$-space between 1 and 100 m, and 5 azimuth / elevation error magnitudes $\log_{10}$-spaced between 0.001 and 0.1 degrees. Overall, the larger the error in either direction, the higher the transition point, indicating that Herrick-Gibbs is more accurate at longer track lengths. This behavior may be explained by the reduction in sensitivity to measurement errors that Herrick-Gibbs exhibited in the error bar plots; e.g., Figure IV.2. Furthermore, the transition point is more sensitive to range errors than angle errors. As a consequence, should range errors be large, it dominates the transition point behavior, as can be seen in the left most column. This result shows that larger errors enable Herrick-Gibbs to be the more accurate method for a longer set of track lengths. More significantly, we can get an idea of which method to use based on the magnitude of the range errors.

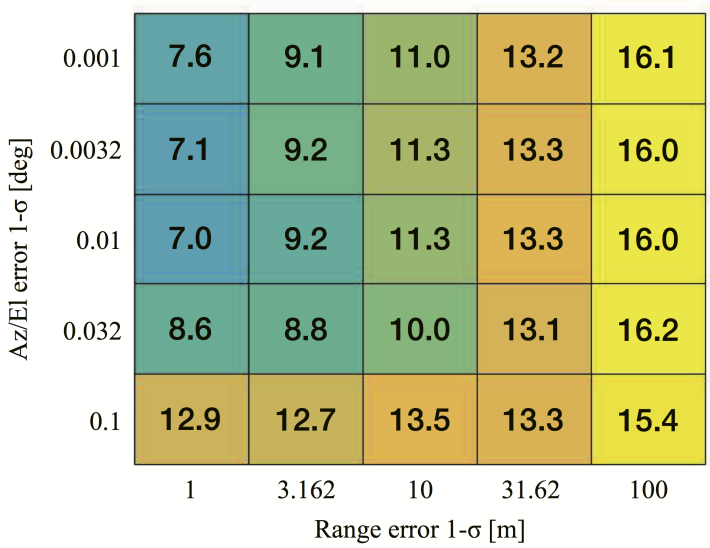

Figure IV.7. Transition point as a function of measurement error magnitude. Blue represents low transition point values, and yellow represents high values.

IV.B. Analytic PDF Results

Figure IV.8 shows a histogram of the $\dot{x}_2$ values found by Monte Carlo, which is a visualization of the PDF. The histogram is normalized so that the sum of all bars is 1. The histogram only contains the values that emulate a 1-D PDF along $\dot{x}_2$. The curve along the histogram shows the analytic PDF values at each value of $\dot{x}_2$. The values are normalized by the total sum of analytic PDF values. This normalization allows us to visualize both analytic and Monte Carlo PDF values on the same scale. The curve falls along the histogram, showing that the Monte Carlo and analytic PDF results are consistent with each other. This validates our Monte Carlo results and strengthens our claim about the robustness of the Herrick-Gibbs method. Furthermore, the consistency between both approaches suggests that the analytic PDF was evaluated correctly. Consistent results are found for Monte Carlo and analytic PDF results for $\dot{y}_2$ and $\dot{z}_2$ as well; see Figure IV.9. All PDF values

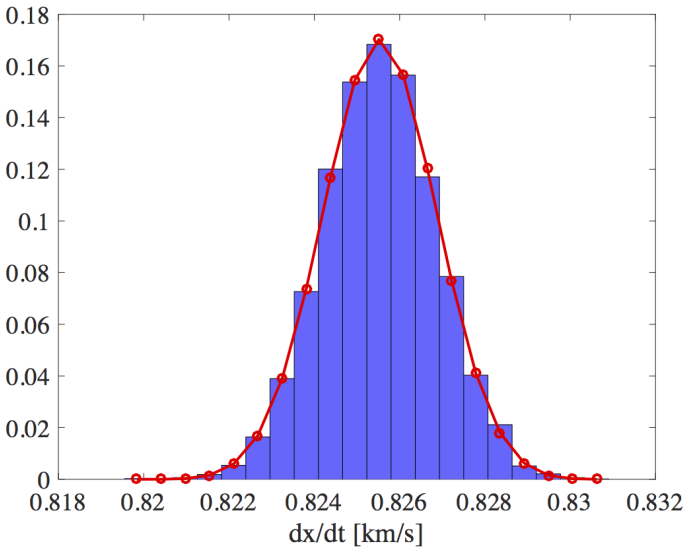

Figure IV.8. Analytic and Monte Carlo PDF vs $\dot{x}$

demonstrate no skewness with a single mode.

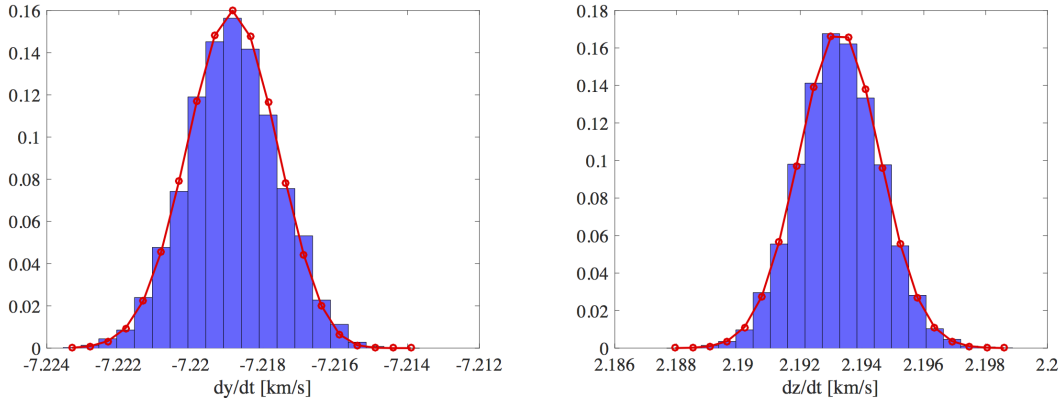

Figure IV.9. Analytic and Monte Carlo PDF vs. $\dot{y}$ and $\dot{z}$

CHAPTER V

CONCLUSIONS

We set out to solve the problem of determining when to switch between using Gibbs and Herrick-Gibbs IOD methods. Having a more accurate initial state estimate will provide more precise orbit determination. We performed a comprehensive statistical analysis of IOD accuracy for both methods using a Monte Carlo and analytic PDF approach. The results provide a greater understanding of the reliability of Gibbs and Herrick-Gibbs methods. For the Monte Carlo test, by introducing measurement errors and varying track length, the overall trends of Gibbs and Herrick-Gibbs performance are tested and determined to be consistent with expectations. We then quantified the transition point that determines the method that is more accurate for a given track length. For the tested orbits, transition points were between 6° to 16°. This result is significant as it was previously suggested to use Herrick-Gibbs for track lengths less than 1°. Instead, Herrick-Gibbs can remain the more accurate method for much larger track lengths. Once the track length passes the transition point, however, Gibbs takes over as the more accurate method.

The effects of orbital parameters on the Gibbs / Herrick-Gibbs transition point were also tested. The results show that, although there is no general behavior of the transition point as a function of target semi-major axis or eccentricity, the behavior of the normalized error vs. track length plot for each individual method can be explained physically. We also determined that the transition point is more sensitive to range error magnitudes compared to azimuth and elevation errors.

Finally, The PDF value for the state estimate provided by Herrick-Gibbs was evaluated both analytically and through Monte Carlo. The PDF was determined by

employing the transformation of variables method along with properties of the Dirac delta function. Both methods were found to be consistent with each other. This result validates the previous results we obtained from our Monte Carlo approach.

For future work, there are further variations to the approach that can be used to evaluate Gibbs and Herrick-Gibbs performance. For example, the location of the middle position vector can be varied to test other positions along the orbit than perigee. Another issue to further investigate is the apparent insensitivity of the Herrick-Gibbs method to measurement errors at longer track lengths. The PDF for the state estimate provided by the Gibbs method could also be evaluated analytically.

REFERENCES

[1] Joint Chiefs of Staff, "Joint Publication 3-14: Space Operations," May 2013.

[2] Curtis, H. D., *Orbital Mechanics for Engineering Students*, Butterworth-Heinemann, Waltham, MA, 3rd ed., 2013.

[3] Schaeperkoetter, A., *A Comprehensive Comparison Between Angles-Only Initial Orbit Techniques*, Master's thesis, Texas A&M University, 2011.

[4] Gibbs, J. W., *On the Determination of Elliptical Orbits from Three Complete Observations*, Vol. 4, Memoires National Academy of Science, 1889.

[5] Vallado, D., *Fundamentals of Astrodynamics and Applications*, Microcosm Press, Hawthorne, CA, 3rd ed., 2007.

[6] Bate, R. M., Mueller, D. D., and White, J. E., *Fundamentals of Astrodynamics*, Dover Publications, New York, 1971.

[7] Herrick, S., *Astrodynamics: Orbit Determination, Space Navigation, Celestial Mechanics*, Vol. 1, Van Nostrand Reinhold Co., London, 1971.

[8] Battin, R. H., *An Introduction to the Mathematics and Methods of Astrodynamics*, AIAA, Reston, VA, revised ed., 1999.

[9] Taff, L. G., "The Resurrection of Laplace's Method of Initial Orbit Determination Methods," Tech. Rep. 628, Lincoln Laboratory, 1983.

[10] Taff, L. G., Randall, P. M. S., and Stansfield, S. A., "Angles-Only, Ground-Based, Initial Orbit Determination," Tech. Rep. 618, Lincoln Laboratory, 1984.

[11] Taff, L. G., "On Initial Determination," *The Astronomical Journal*, Vol. 89, No. 9, 1984, pp. 1426–1428.

[12] Celletti, A. and Pinzari, G., "Four Classical Methods for Determining Planetary Elliptic Elements: A Comparison," *Celestial Mechanics and Dynamical Astronomy*, Vol. 93, No. 1, September 2005, pp. 1–52.

[13] Celletti, A. and Pinzari, G., *Periodic, Quasi-Periodic and Chaotic Motions in Celestial Mechanics: Theory and Applications*, chap. Dependence on the Observational Time Intervals and Domain of Convergence of Orbital Determination Methods, Springer Netherlands, 2006.

[14] Fadrique, F., Mate, A., Grau, J., Sanchez, J., and Garcia, L., "Comparison of Angles Only Initial Orbit Determination Algorithms for Space Debris Cataloguing," 2011, Presented at the *2011 International Symposium on Space Flight Dynamics*.

[15] Foster, B., *Orbit Determination for a Microsatellite Rendezvous with a Non-Cooperative Target*, Master's thesis, Air Force Institute of Technology, 2003.

[16] Weisman, R. M., Majji, M., and Alfriend, K. T., "Analytic Characterization of Measurement Uncertainty and Initial Orbit Determination on Orbital Element Representation," *Celestial Mechanics and Dynamical Astronomy*, Vol. 118, No. 2, 2014, pp. 165–195.

[17] Crassidis, J. L. and Junkins, J. L., *Optimal Estimation of Dynamic Systems*, Taylor and Francis Group, Boca Raton, FL, 2012.

[18] Au, C. and Tam, J., "Transforming Variables using the Dirac Generalized Function," *The American Statistician*, Vol. 53, No. 3, August 1999.

APPENDIX A

d VS. TRACK LENGTH PLOTS

For each satellite tested, a log-y plot of the mean d vs. track length for both IOD methods (top) as well as individual error bar plots for Gibbs (left) and Herrick-Gibbs (right) are given. As in the main text, the lines represent the mean d value, where as bars represent the range of d values for each track length based on measurement error.

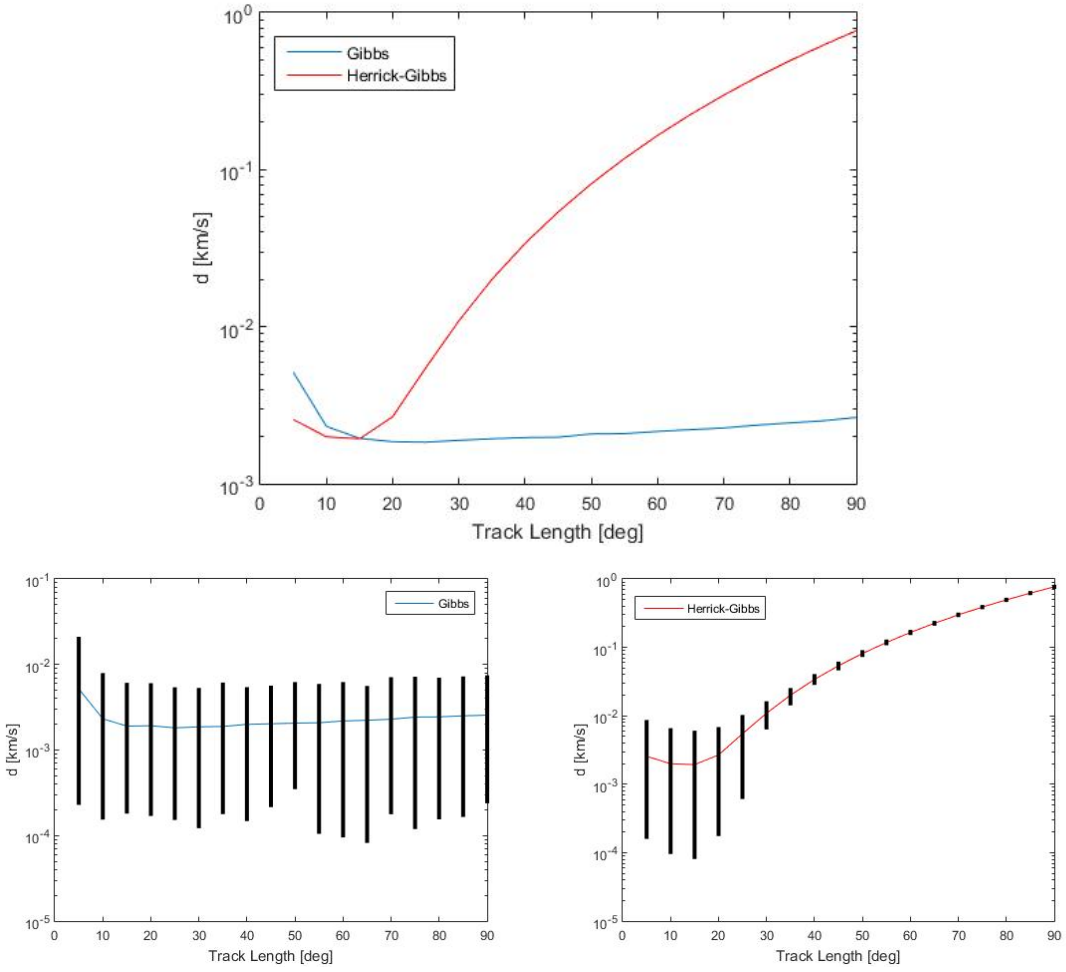

Figure A.1. Comparison of IOD performance for GeoEye-1.

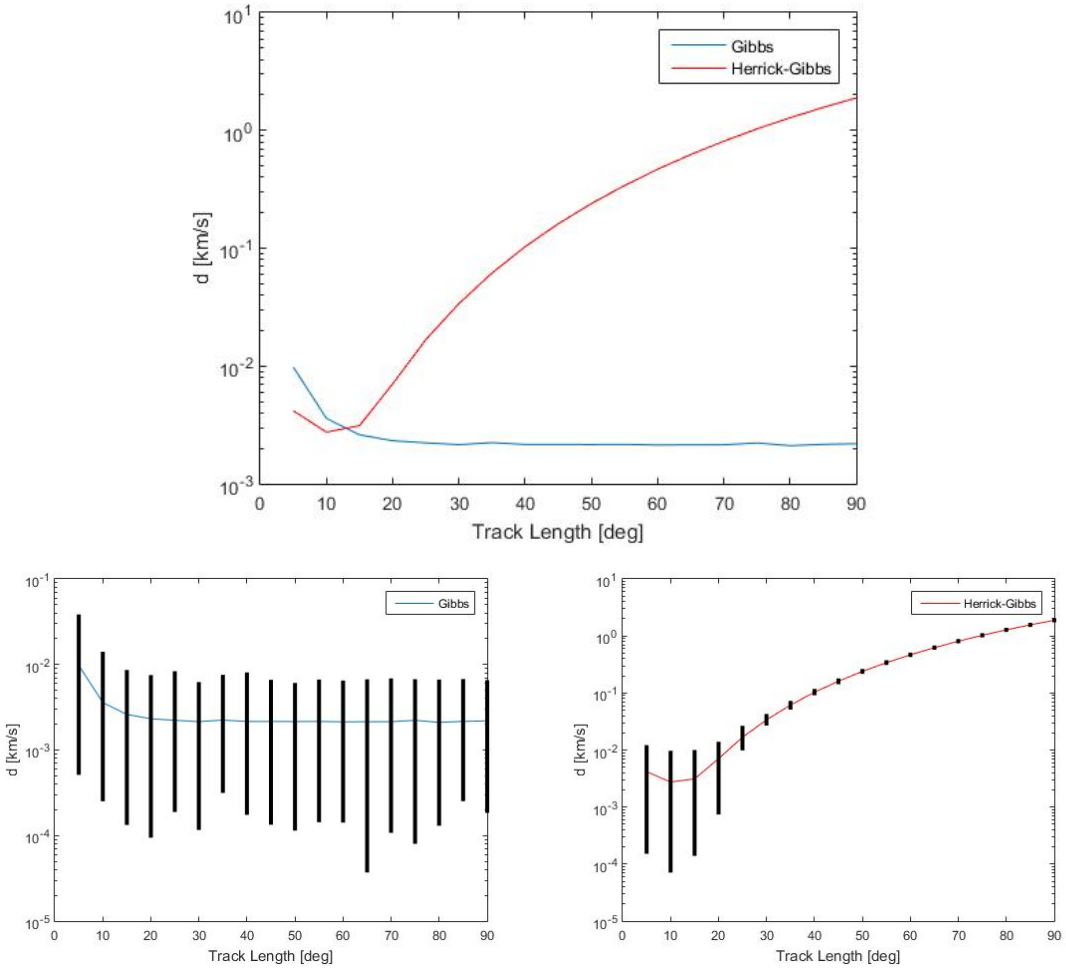

Figure A.2. Comparison of IOD performance for Molniya.

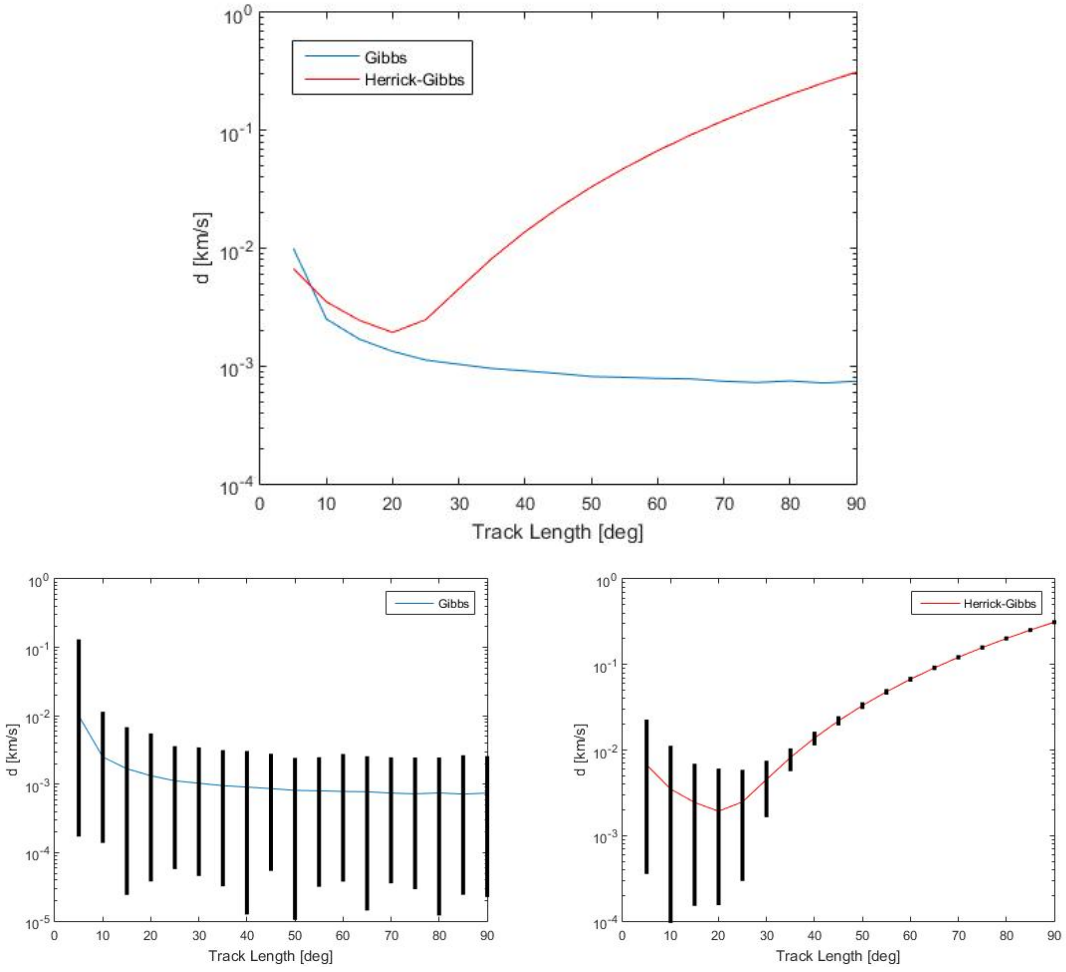

Figure A.3. Comparison of IOD performance for Geostationary.

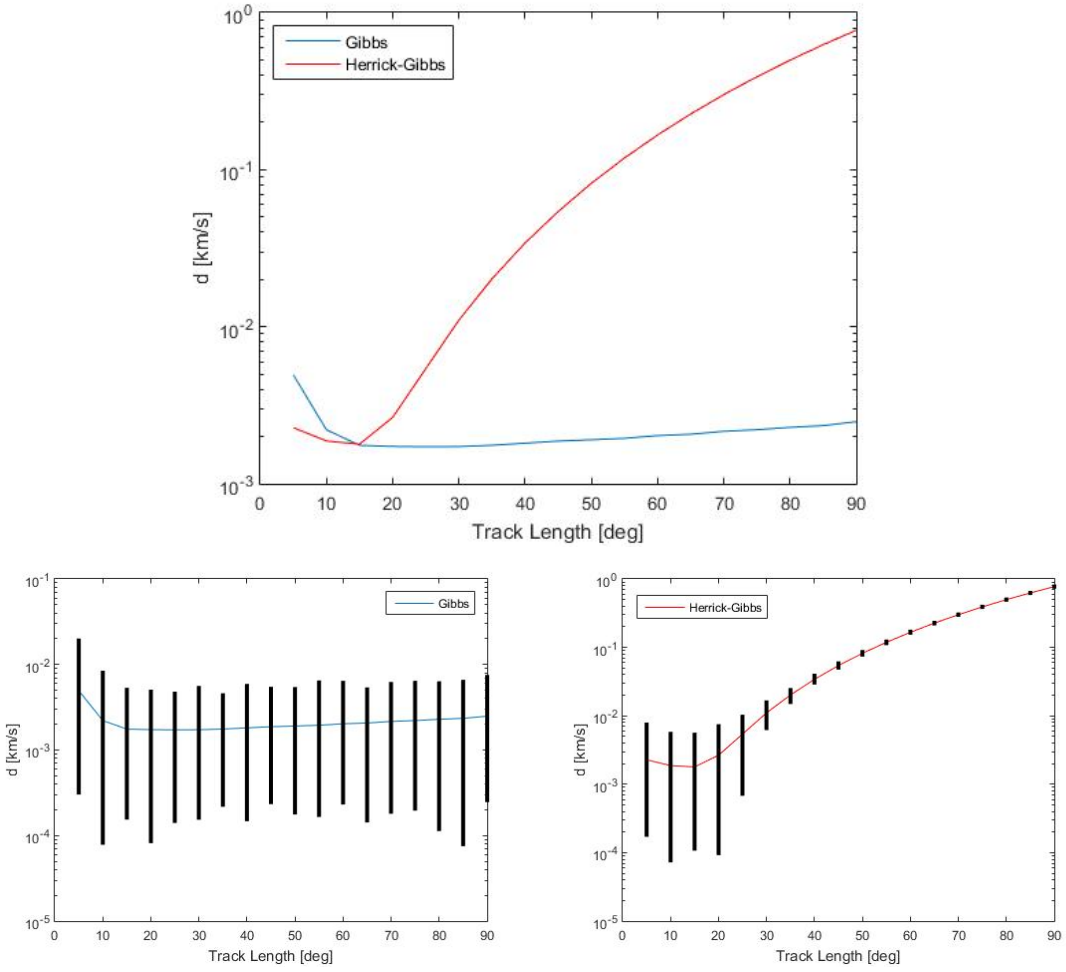

Figure A.4. Comparison of IOD performance for Hubble.

APPENDIX B

IOD METHOD DERIVATIONS

B.1. Gibbs Derivation

If three position vectors are coplanar $(\mathbf{r}_1, \mathbf{r}_2, \mathbf{r}_3)$, there exists 3 constants that satisfy the expression:

$$c_1\mathbf{r}_1 + c_2\mathbf{r}_2 + c_3\mathbf{r}_3 = \mathbf{0} \tag{B.1}$$

Crossing this term with each position vector, yields the following expressions:

$$c_2(\mathbf{r}_1 \times \mathbf{r}_2) = c_3(\mathbf{r}_3 \times \mathbf{r}_1) \tag{B.2}$$

$$c_1(\mathbf{r}_1 \times \mathbf{r}_2) = c_3(\mathbf{r}_2 \times \mathbf{r}_3) \tag{B.3}$$

$$c_1(\mathbf{r}_3 \times \mathbf{r}_1) = c_2(\mathbf{r}_2 \times \mathbf{r}_3) \tag{B.4}$$

Dot Equation (B.1) with the eccentricity vector $\mathbf{e}$:

$$c_1(\mathbf{e} \cdot \mathbf{r}_1) + c_2(\mathbf{e} \cdot \mathbf{r}_2) + c_3(\mathbf{e} \cdot \mathbf{r}_3) = 0 \tag{B.5}$$

This step will allow us to get an expression with the position vectors in terms of the semiparameter p. Recalling that the angle between the eccentricity and position vector is the true anomaly, we can use the expression:

$$\mathbf{e} \cdot \mathbf{r} = er\cos f \tag{B.6}$$

To get a new expression from the trajectory equation:

$$p = r(1 + e\cos f) = r + re\cos f = r + \mathbf{e} \cdot \mathbf{r} \Leftrightarrow \mathbf{e} \cdot \mathbf{r}_i = p - r_i \tag{B.7}$$

Using Equation (B.7) in Equation (B.5) yields:

$$c_1(p - r_1) + c_2(p - r_2) + c_3(p - r_3) = 0 \tag{B.8}$$

Multiply this by $\mathbf{r}_3 \times \mathbf{r}_1$:

$$c_1(p - r_1)(\mathbf{r}_3 \times \mathbf{r}_1) + c_2(p - r_2)(\mathbf{r}_3 \times \mathbf{r}_1) + c_3(p - r_3)(\mathbf{r}_3 \times \mathbf{r}_1) = \mathbf{0} \tag{B.9}$$

Substituting in Equations (B.2) and (B.4) to express the previous equation in terms of the constant c_2:

$$c_2(p - r_1)(\mathbf{r}_2 \times \mathbf{r}_3) + c_2(p - r_2)(\mathbf{r}_3 \times \mathbf{r}_1) + c_2(p - r_3)(\mathbf{r}_1 \times \mathbf{r}_2) = \mathbf{0} \tag{B.10}$$

Dividing out c_2:

$$p(\mathbf{r}_1 \times \mathbf{r}_2 + \mathbf{r}_2 \times \mathbf{r}_3 + \mathbf{r}_3 \times \mathbf{r}_1) = r_1(\mathbf{r}_2 \times \mathbf{r}_3) + r_2(\mathbf{r}_3 \times \mathbf{r}_1) + r_3(\mathbf{r}_1 \times \mathbf{r}_2) \tag{B.11}$$

We can define the right side of Equation (B.11) as $\mathbf{N}$ and the the vector part of the left side as $\mathbf{D}$

$$\mathbf{D} = \mathbf{r}_1 \times \mathbf{r}_2 + \mathbf{r}_2 \times \mathbf{r}_3 + \mathbf{r}_3 \times \mathbf{r}_1 \tag{B.12}$$

$$\mathbf{N} = r_1(\mathbf{r}_2 \times \mathbf{r}_3) + r_2(\mathbf{r}_3 \times \mathbf{r}_1) + r_3(\mathbf{r}_1 \times \mathbf{r}_2) = p\mathbf{D} \tag{B.13}$$

$\mathbf{N}$ and $\mathbf{D}$ have the same direction which is the direction of the angular momentum vector $\mathbf{h}$. This is also the direction of $\hat{\mathbf{W}}$ in the perifocal coordinate system. The $\hat{\mathbf{P}}$ vector from the perifocal frame points towards periapsis, like the eccentricity vector. $\hat{\mathbf{W}}$ and $\hat{\mathbf{P}}$ can be expressed as:

$$\hat{\mathbf{W}} = \frac{\mathbf{N}}{|\mathbf{N}|} \tag{B.14}$$

$$\hat{\mathbf{P}} = \frac{\mathbf{e}}{|\mathbf{e}|} \tag{B.15}$$

Since $\hat{\mathbf{W}}$ and $\hat{\mathbf{P}}$ are orthogonal, we can define a third vector $\hat{\mathbf{Q}}$ as:

$$\hat{\mathbf{Q}} = \hat{\mathbf{W}} \times \hat{\mathbf{P}} = \frac{\mathbf{N} \times \mathbf{e}}{|\mathbf{N}||\mathbf{e}|} \tag{B.16}$$

Substituting the definition of $\mathbf{N}$ from Equation (B.13) into this expression gives:

$$Ne\hat{\mathbf{Q}} = \mathbf{N} \times \mathbf{e} = r_1[(\mathbf{r}_2 \times \mathbf{r}_3) \times \mathbf{e}] + r_2[(\mathbf{r}_3 \times \mathbf{r}_1) \times \mathbf{e}] + r_3[(\mathbf{r}_1 \times \mathbf{r}_2) \times \mathbf{e}] \quad \text{(B.17)}$$

Then, using the general relationship for triple cross products of vectors:

$$(\mathbf{a} \times \mathbf{b}) \times \mathbf{c} = (\mathbf{a} \cdot \mathbf{c})\mathbf{b} - (\mathbf{b} \cdot \mathbf{c})\mathbf{a} \quad \text{(B.18)}$$

Equation (B.17) can be simplified to:

$$Ne\hat{\mathbf{Q}} = r_1(\mathbf{r}_2 \cdot \mathbf{e})\mathbf{r}_3 - r_1(\mathbf{r}_3 \cdot \mathbf{e})\mathbf{r}_2 + r_2(\mathbf{r}_3 \cdot \mathbf{e})\mathbf{r}_1 - r_2(\mathbf{r}_1 \cdot \mathbf{e})\mathbf{r}_3 + r_3(\mathbf{r}_1 \cdot \mathbf{e})\mathbf{r}_2 - r_3(\mathbf{r}_2 \cdot \mathbf{e})\mathbf{r}_1 \quad \text{(B.19)}$$

Using Equation (B.7) once again and factoring p from the right side gives us:

$$Ne\hat{\mathbf{Q}} = p[(r_2 - r_3)\mathbf{r}_1 + (r_3 - r_1)\mathbf{r}_2 + (r_1 - r_2)\mathbf{r}_3] = p\mathbf{S} \quad \text{(B.20)}$$

Where $\mathbf{S}$ is defined by the bracketed quantity in (B.20). $\hat{\mathbf{Q}}$ and $\mathbf{S}$ must be in the same direction which makes it possible to write $Ne = pS$ since the magnitudes must be equal. This allows us to express:

$$e = \frac{S}{D} \quad \text{(B.21)}$$

Since $\hat{\mathbf{P}}$, $\hat{\mathbf{Q}}$ and $\hat{\mathbf{W}}$ are orthogonal:

$$\hat{\mathbf{P}} = \hat{\mathbf{Q}} \times \hat{\mathbf{W}} \quad \text{(B.22)}$$

We can use the defined $\mathbf{N}$, $\mathbf{D}$, and $\mathbf{S}$ vectors to define the velocity at the middle time, $\dot{\mathbf{r}}_2$. First, we start with the following expression for $\dot{\mathbf{r}}_2$:

$$\dot{\mathbf{r}}_2 \times \mathbf{h} = \mu \left[\frac{\mathbf{r}_2}{r_2} + \mathbf{e} \right] \quad \text{(B.23)}$$

Crossing both sides by the angular momentum vector, $\mathbf{h}$ yields:

$$\mathbf{h} \times (\dot{\mathbf{r}}_2 \times \mathbf{h}) = \mu \left[\frac{\mathbf{h} \times \mathbf{r}_2}{r_2} + \mathbf{h} \times \mathbf{e} \right] \quad \text{(B.24)}$$

Once again using the cross product identity in Equation (B.18), this expression can be simplified to:

$$h^2\dot{\mathbf{r}}_2 = \mu\left[\frac{\mathbf{h}\times\mathbf{r}_2}{r_2} + \mathbf{h}\times\mathbf{e}\right] \tag{B.25}$$

We can then write $\mathbf{h} = h\hat{\mathbf{W}}$ and $\mathbf{e} = e\hat{\mathbf{P}}$ and express the velocity as:

$$\dot{\mathbf{r}}_2 = \frac{\mu}{h}\left[\frac{\hat{\mathbf{W}}\times\mathbf{r}_2}{r_2} + e\hat{\mathbf{W}}\times\hat{\mathbf{P}}\right] = \frac{\mu}{h}\left[\frac{\hat{\mathbf{W}}\times\mathbf{r}_2}{r_2} + e\hat{\mathbf{Q}}\right] \tag{B.26}$$

Using $N = pD$ and $h = \sqrt{p\mu}$ allows us to express the angular momentum magnitude as:

$$h = \sqrt{\frac{N\mu}{D}} \tag{B.27}$$

Using this expression along with $e = S/D$, $\hat{\mathbf{Q}} = \mathbf{S}/S$ and $\hat{\mathbf{W}} = \mathbf{D}/D$ gives the final expression for the velocity:

$$\dot{\mathbf{r}}_2 = \frac{1}{r_2}\sqrt{\frac{\mu}{ND}}(\mathbf{D}\times\mathbf{r}_2) + \sqrt{\frac{\mu}{ND}}\mathbf{S} = \sqrt{\frac{\mu}{ND}}\left[\frac{\mathbf{D}\times\mathbf{r}_2}{r_2} + \mathbf{S}\right] \tag{B.28}$$

The Gibbs method does use any approximations and is a geometric approach to determine the exact velocity at the second epoch. It falls short if the position vectors are too closely spaced or affected by measurement errors as the $\mathbf{D}$ vector is poorly determined from Equation (B.12).

B.2. Herrick-Gibbs Derivation

Defining three position vectors $(\mathbf{r}_1, \mathbf{r}_2, \mathbf{r}_3)$ and their times of observation (t_1, t_2, t_3), allow us to define the following power series expansions up to the fifth order:

$$\mathbf{r} = \mathbf{a}_0 + t\mathbf{a}_1 + t^2\mathbf{a}_2 + t^3\mathbf{a}_3 + t^4\mathbf{a}_4 + t^5\mathbf{a}_5 \tag{B.29}$$

$$\mathbf{v} = \mathbf{a}_1 + 2t\mathbf{a}_2 + 3t^2\mathbf{a}_3 + 4t^3\mathbf{a}_4 + 5t^4\mathbf{a}_5 \tag{B.30}$$

$$-\frac{\mu}{r^3}\mathbf{r} = 2\mathbf{a}_2 + 6t\mathbf{a}_3 + 12t^2\mathbf{a}_4 + 20t^3\mathbf{a}_5 \tag{B.31}$$

The last expression uses the equation of motion of the two-body problem to replace the acceleration term. The $\mathbf{a}_n$ terms are time independent unknowns from the power series. Next, we define the following terms as the difference between the times of observation:

$$\Delta t_{32} = t_3 - t_2 \tag{B.32}$$

$$\Delta t_{31} = t_3 - t_1 \tag{B.33}$$

$$\Delta t_{21} = t_2 - t_1 \tag{B.34}$$

We can replace the t terms in the power series and get the following set of equations:

$$\mathbf{r}_1 = \mathbf{a}_0 - \Delta t_{21}\mathbf{a}_1 + \Delta t_{21}^2\mathbf{a}_2 - \Delta t_{21}^3\mathbf{a}_3 + \Delta t_{21}^4\mathbf{a}_4 - \Delta t_{21}^5\mathbf{a}_5 \tag{B.35}$$

$$\mathbf{r}_2 = \mathbf{a}_0 \tag{B.36}$$

$$\mathbf{r}_3 = \mathbf{a}_0 - \Delta t_{32}\mathbf{a}_1 + \Delta t_{32}^2\mathbf{a}_2 - \Delta t_{32}^3\mathbf{a}_3 + \Delta t_{32}^4\mathbf{a}_4 - \Delta t_{32}^5\mathbf{a}_5 \tag{B.37}$$

$$\mathbf{v}_2 = \mathbf{a}_1 \tag{B.38}$$

$$-\frac{\mu}{r_1^3}\mathbf{r}_1 = 2\mathbf{a}_2 - 6\Delta t_{21}\mathbf{a}_3 + 12\Delta t_{21}^2\mathbf{a}_4 - 20\Delta t_{21}^3\mathbf{a}_5 \tag{B.39}$$

$$-\frac{\mu}{r_2^3}\mathbf{r}_2 = 2\mathbf{a}_2 \tag{B.40}$$

$$-\frac{\mu}{r_3^3}\mathbf{r}_3 = 2\mathbf{a}_2 + 6\Delta t_{32}\mathbf{a}_3 + 12\Delta t_{32}^2\mathbf{a}_4 + 20\Delta t_{32}^3\mathbf{a}_5 \tag{B.41}$$

We can immediately eliminate $\mathbf{a}_0, \mathbf{a}_1$, and $\mathbf{a}_2$ and reduce the system to four equations solving for four vector unknowns $(\mathbf{a}_3, \mathbf{a}_4, \mathbf{a}_5, \mathbf{v}_2)$. When $\Delta t_{32} = \Delta t_{21}$, however, the $\mathbf{v}_2$ term cancels out and we cannot find a direct solution. We can get around this by first reducing our power series approximation to the fourth order. Then, we eliminate the $\mathbf{a}_2$ terms in Equations (B.35) and (B.37) by multiplying them by Δt_{32} and Δt_{21},

respectively, and subtracting. The resulting equation is:

$$\begin{aligned}\Delta t_{32}^2\mathbf{r}_1 - \Delta t_{21}^2\mathbf{r}_3 = (\Delta t_{32} - \Delta t_{21})\Delta t_{31}\mathbf{a}_0 \\ - \Delta t_{32}\Delta t_{31}\Delta t_{21}\mathbf{a}_1 - \Delta t_{32}^2\Delta t_{31}\Delta t_{21}^2\mathbf{a}_3 \\ + \Delta t_{32}^2\Delta t_{31}\Delta t_{21}^2(\Delta t_{21} - \Delta t_{32})\mathbf{a}_4 \quad \text{(B.42)}\end{aligned}$$

Equation (B.42) is used in place of (B.35) and (B.37). We now have 6 equations for 6 unknowns $(\mathbf{a}_0, \mathbf{a}_1, \mathbf{a}_2, \mathbf{a}_3, \mathbf{a}_4, \mathbf{v}_2)$. We can then solve directly for $\mathbf{v}_2$:

$$\begin{aligned}\mathbf{v}_2 = -\Delta t_{32}\left[\frac{1}{\Delta t_{21}\Delta t_{31}} + \frac{\mu}{12r_1^3}\right]\mathbf{r}_1 + (\Delta t_{32} - \Delta t_{21})\left[\frac{1}{\Delta t_{21}\Delta t_{32}} + \frac{\mu}{12r_2^3}\right]\mathbf{r}_2 \\ + \Delta t_{21}\left[\frac{1}{\Delta t_{32}\Delta t_{31}} + \frac{\mu}{12r_3^3}\right]\mathbf{r}_3. \quad \text{(B.43)}\end{aligned}$$